Boosting ultrathin aSi-H solar cells absorption through a nanoparticle cross-packed metasurface

Mahmoud H. Elshorbagy[a,b], Eduardo López-Fraguas[a], José Manuel Sánchez-Pena[a], Braulio García-Cámara[a], Ricardo Vergaz[a,*]

[a] GDAF-UC3M, Dep. Tecnología Electrónica, Universidad Carlos III de Madrid, Avda. Universidad, 30. Leganés, Madrid, Spain
[b] Physics Department, Faculty of Science, Minia University, 61519 El-Minya, Egypt

ARTICLE INFO

ABSTRACT

Hydrogenated amorphous silicon (a-Si:H) solar cells have some performance limitations related to the mobility and lifetime of their carriers. For this reason, it is interesting to explore thin-film solutions, achieving a tradeoff between photons optical absorption and the electrical path of the carriers to get the optimum thickness. In this work, we propose the insertion of a metasurface based on a cross-patterned ITO contact film, where the crosses are filled with nanospheres. We numerically demonstrate that this configuration improves the photogenerated current up to a 40% by means of the resonant effects produced by the metasurface, being independent on the impinging light polarization. Light handling mechanisms guide light into the active and auxiliary layers, increasing the effective absorption and mitigating the Staebler-Wronski effect. The selection of optimum materials and parameters results in nanospheres of ZnO with a 220 nm radius.

1. Introduction

Metasurfaces based on nano-elements that can tune their optical response by changing their materials and geometries have been a matter of interest in the last years, for increasing both the emission and absorption of light at certain wavelengths (Vaskin et al., 2019; Zou et al., 2019). While traditionally focused on metallic nanoplasmonics using different shapes and geometries (Atwater and Polman, 2010; Khan et al., 2019), the study has recently been oriented to dielectric nanostructures supporting Mie resonances (Spinelli et al., 2012). The reasons are their low absorption losses and their easy integration in diverse solar cells and semiconductor-based emitters (Brongersma et al., 2014; Vismara et al., 2019; Therekov et al., 2019; Barreda et al., 2019b; Algorri et al., 2019; Elshorbagy et al., 2019). Spin-coated silica nanospheres producing an antireflection coating and increasing PCE a 6.8% (Luo et al., 2018), or cross-shaped dielectric nanoresonators for color displays (Vashistha et al., 2017) are some examples. The resonances are tuned by an adequate selection of materials and geometries (Enrichi et al., 2018).

We base our proposal on theoretical and numerical studies where promising previous results were found. Barreda et al. (2019) numerically deduce that parallelepiped nanoparticles obtain the best light directionality, but all the analysis is made on air, and the conditions vary when the substrate changes. On the contrary, Li et al. (2019) successfully simulate a 200 nm thin film solar cell including 500 nm-spherical TiO$_2$ nanoparticles which are embedded 90 nm into the top silicon layer. The authors claimed that their proposal absorbs 3.15 times more light than a planar structure after optimizing the materials to have a remarkably low-losses and forward scattering condition.

Cross-shaped resonant elements have been widely explored in the bibliography about metasurfaces, even for enhancing light emission (Vaskin et al., 2019). They have been used as perfect absorbers, spectrally tunable by the dimensions of crosses (Cao et al., 2019), or as plasmonic UV and IR filters to avoid solar cell degradation. In this latter case, Khoshdel et al. (2019) showed that their effect is polarization-independent.

In terms of the ability of placing the nanoparticles, examples can be found by spin coating on a nanometer-scale pattern made by interferometric lithography (Xia and Brueck, 2004) or by nanoparticles-on-grooves (Son et al., 2009). Furthermore, examples of nanospheres layers improving solar cells performance can also be found in the work of Grandidier et al. (2012), by a 700 nm-radius hexagonal periodic arrangement of lossless dielectric resonant nanospheres, improving 11% the PCE of a 100-nm GaAs solar cell, or in the one of Wang et al. (2016), by resonant nanospheres placed on the ITO layer of an ultrathin silicon solar cell, to improve the absorption in a 26.5% by propagating

---

light down into the active layer.

On the other hand, Lee and Ha (2011) nanostructured the ITO layer film, used in this case in a liquid crystal device. It was made by a nanoimprint method with a PDMS mold over spin-coated all-solution ITO nanoparticles. The resulted ITO film had 200 Ω/sq and 80% transmittance. In addition, the work by Jang et al. (2016) provides a 3-D flower-nanopatterning technique combining ion-assisted aerosol and soft lithography, and replication through a polymeric mold, on a TiO₂ layer acting as electron transport layer for perovskite solar cells. They achieved an increase in the light harvesting efficiency from 400 to 800 nm and took advantage of the improvement in charge collection due to the nanostructure. Ha et al. (2016) extended the application of this method to silicon solar cells.

This kind of structures is as more efficient as closer to the active layer. Thus, thin film solar cells are promising devices to use them. We can focus our attention on hydrogenated a-Si (a-Si:H) thin-film solar cell, due to this material abundance and nontoxicity. However, the low mobility and short lifetime of charge carriers in this kind of solar cell are still a drawback. Thus, the thickness of the devices of the state of art marks an upper limit around 350 nm. Reducing the thickness increases the probability of carrier collection (Könenkamp et al., 1990). Another challenge is the Staebler–Wronski effect (SWE), which is a degradation induced by light exposure (Staebler and Wronski, 1977). Fortunately, this effect can be recovered by an annealing process (Agarwal and Omar, 2018). The efficiency of an a-Si:H solar cell can be returned to its initial state if the cell is annealed at 150 °C for four hours (Staebler and Wronski, 1977), or annealing at lower temperatures (e.g. at 80 °C) over extended times (Pola et al., 2008). Even light induced annealing could partially compensate the SWE defects (Fujikake et al., 1994), as solar cell temperature under operation could reach values of 50 °C to 60 °C (Dhouib and Filali, 1990). Therefore, if a strategy improves also the absorption in the auxiliary layers that form the cell, it can increase even more the temperature inside the cell, and compensate the defects produced by SWE.

In this paper, we explore a combination of two approaches to enhance the performance of a hydrogenated amorphous silicon (a-Si:H) solar cell: a pattern based on cross-shaped grooves, and their filling with dielectric nanospheres. Each one of these elements separately can increase light absorption in the active layer, and thus enhance the silicon solar cell performance. Both show promising previous results in literature. Our goal is to numerically show that their combination can boost their effects and produces a remarkable increase in the performance of a thin-film solar cell.

2. Design parameterizations and methods

As pointed out above, our proposal combines a cross 2D pattern in the ITO top contact and its filling with dielectric nanoparticles. The crossed pattern guarantees polarization insensitive effects, close to the real illumination. We will explore the dimensions of the cross and the composition of the nanoparticles to achieve the optimum performance, using active layers with a thickness ranging from 50 nm to the 350 nm, which is the limit of planar cells as stated above.

2.1. Design parameterizations

The conventional design for planar thin film aSi-H solar cell has the following form: a back mirror [200 nm]/ an AZO (Aluminum-doped Zinc Oxide) contact layer [100 nm]/n-doped a-Si-H [22 nm]/intrinsic a-Si-H [350 nm]/p-doped a-Si-H [17 nm]/an ITO (Indium Tin Oxide) contact layer [70 nm] (based on: Shiri et al., 2019; Amalatas and Alkaisi, 2019; Morawiec et al., 2019). The schematic diagram of this device is depicted in Fig. 1a. However, our first step is reducing the drawbacks of having a thick layer. In this sense, hereinafter we select a value under the 350 nm upper limit mentioned in the Introduction (150 nm). To compensate the decrease in absorption by this reduction,
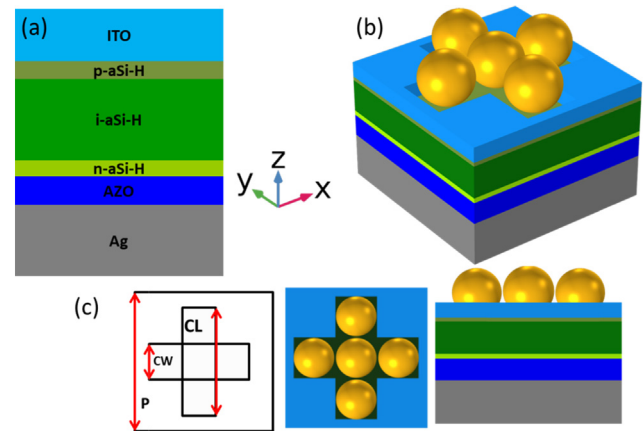

Fig. 1. (a) Schematic diagram of the planar cell having a flat top contact from ITO. (b) 3D diagram of the device with the nanostructure integrated on the top composed of ITO pattern filled with dielectric nanospheres. (c) Top and side cross-sections of the device with nanostructure, the cross-section on the left contains the geometrical parameters of the ITO pattern, the middle and right ones show how it is filled with spheres.

we propose the addition of a metasurface, which unit cell is shown in Fig. 1.b, and deconstructed and dimensioned in Fig. 1.c. A pattern based on a cross shape is etched in the ITO layer, with a pitch period P, a length CL and a width CW. Additionally, we insert five nanospheres in the cross as shown in Fig. 1b. This configuration provides broadband dipolar effects, coming from the cross pattern and the nanospheres.

For the sake of simplicity in the optimization of the geometrical parameters, we link the cross dimensions with the sphere radius, R. This is because the spheres would fill the grooves only if their diameter is slightly smaller than the groove width ($2R < CW$). For this reason, we have considered a tolerance value, so that $CW = 2R + 10$ nm. For the groove length, we insert only 3 spheres, because it is the minimum value to fit the nanospheres in a cross-shape. At the same time, it reduces not only the cell size to a minimum, but also the complexity of the system, as well as the related computational cost to optimize it. The pattern in ITO has a period P, where $P = CL + S$, being S the separation between the crosses.

2.2. Methods

COMSOL Multiphysics simulation package, based on the Finite Element Method (FEM), is used to compute the distribution of the optical fields into each layer of the cell by solving Maxwell equations. The model setup is following described. An illumination source is used to generate a plane wave which spectral power resembles the AM1.5 standard of the solar irradiance (NREL, 2019). The domain in which the computation is performed is the unit cell described in Fig. 1. Periodic boundary conditions are implemented in both sides of the unit cell to account for the full device. A measuring port is placed below the whole structure, with the proper orientation according to the incident wave conditions. Both input and output ports serve to calculate the total reflection and total transmission of the system. A built-in function based on the distribution of the optical fields and the complex optical constants of each material is used to calculate the spectral absorbed power for each layer (Boroumand et al., 2016):

$$P(\omega) = \frac{1}{2}\omega\varepsilon''(\omega)|E(\omega)|^2, \tag{1}$$

where ω is the angular frequency of the incoming radiation, ε'' is the imaginary part of the dielectric permittivity of the material, and $|E(\omega)|^2$ is the intensity of the electric field inside that material. The volume integration of this spectral absorption power along the active layers provides the total absorbed power. Dividing it by the input power, we

get the absorption rate of the device, $A(\lambda)$. By assuming that each absorbed photon creates an electron-hole pair; we can obtain the upper limit of the photo-generated short-circuit current density, J_{SC}, through:

$$J_{SC} = \int q \frac{\lambda}{hc} A(\lambda) \phi_{AM1.5}(\lambda) d\lambda, \qquad (2)$$

where q is the charge of the electron, c is the speed of light in vacuum, h is the Planck's constant, $\phi_{AM1.5}(\lambda)$ is the standard solar spectral irradiance, and the integration is done over the whole solar spectrum.

3. Results and discussion

According to the previous section, we evaluate the performance of our device in terms of the short-circuit current density (J_{SC}). In addition, and in order to obtain a reference, we firstly simulate the planar structure of Fig. 1a, according to the method described in the previous section. As we have explained above, we will use an active layer of 150 nm, and the simulation of the planar structure with this active layer and its optical constants (Vora et al., 2014) produces a J_{SC} of 9.14 mA/cm². Hereinafter, we are going to compare every result to this one.

Notwithstanding other possibilities, in this work we focus our attention in two parameters of the proposed device (Fig. 1b): the sphere radius, R, and the refractive index, n, of the material for the nanospheres. While the first one also determines the geometrical properties of the crosses, as was previously explained, the second one is relevant to excite convenient resonant effects. It is important to remark that we firstly consider only the real part of n in order to find the values producing the best performance of our device. Later, we consider the complex refractive index of realistic materials matching these values to obtain the optimum design and numerical performance of our device.

We scan for the optimized metasurfaces geometrical parameters (R and n), fixing the separation between crosses to $S = 100$ nm to simplify the optimization process. After that, we will check S effect too. Fig. 2a shows a map of the simulated short-circuit current density in the active layer as a function of both the sphere radius (R) and the real part of the refractive index (n). A constant index with wavelength is assumed to perform this sweep, because the indices of the usual dielectric materials for the nanospheres are almost constant in the considered part of the spectrum. There are several highlighted regions depending on their performance. We can infer from region 3, for instance, that any combination with low refractive index or small spheres will not increase the value of J_{SC}, because this material and geometry dimensions combination cannot produce Mie resonances in the visible region.

In contrast, regions 2 and 4 show moderate improvements, because of the efficient excitation of Mie resonant effects in a broadband response, mainly associated to the nanoparticles (García-Cámara et al., 2013). However, we have obtained even better values in the region marked as 1, where J_{SC} overcomes the 12 mA/cm² value. This area

comprises sphere radii over 180 nm, and refractive indices from 1.75 to 2.5. In this case, multipolar and diffraction effects coming from the nanoparticles arrangement (Algorri et al., 2017) and the engraved crosses overlap the previous Mie resonances, boosting light absorption in the active layer. To be more accurate, we provide the maximum value for the short-circuit current density as 12.87 mA/cm². This supposes a remarkable enhancement compared with the planar structure. In particular, it is a 40.8% larger than that of the planar device. This value is obtained considering the following parameters of the proposed metasurface: $R = 210$ nm, which leads to the following crosses dimensions: $P = 1390$ nm, $CW = 430$ nm, $CL = 1290$ nm; and $n = 2$. This refractive index is the one of a material such as SiN$_x$, which could be a good candidate for manufacturing the spheres.

In a realistic case, this specific radius could be difficult to obtain, and the refractive index should be one of a realistic material. Fortunately, we have a wide region where the enhancement respect to the planar case is remarkable. In this sense and in order to have the widest tolerance, hereinafter we consider using $R = 220$ nm, and $n = 1.95$ corresponding to the real part of the refractive index of ZnO (Bodurov et al., 2016). This material could be feasibly synthesized by different methods and are commonly used for different applications (Agarwal et al., 2017; Zaidi et al., 2019). In this case, the cross parameters are $P = 1450$ nm, $CW = 450$ nm and $CL = 1350$ nm. Under these conditions and taking into account the complex refractive index of ZnO, J_{SC} achieves a value of 12.8 mA/cm², providing an enhancement of a 40% respect to the planar case. This small difference validates our optimization procedure and its assumptions.

While we described previously that the separation between the crosses is fixed, we want to show that this assumption is not important in the operation of the device. In this sense, we show in Fig. 2b a plot for our optimized case, in which only the parameter S is varied from 50 to 500 nm. As it can be seen, J_{SC} is hardly dependent on S for values between $S = 50$ to $S = 200$ nm, and that it decays for longer separations. This shows that for distances larger than 200 nm the coupling between the neighboring crosses decreases. It proves that coupling phenomena are important to generate the previous multipolar and diffraction effects. At the same time, the effect can be maintained in a convenient range of S, which fortunately ease the fabrication. Notwithstanding, the effect due to the nanoparticles by themselves is still relevant, as the value of the current density in the studied S range is far better than the one in the planar case. Specific, it is remarkable that when S gets a high value, around 500 nm, the enhancement is still relevant. Indeed, J_{SC} holds on a 11.85 mA/cm², which is still a 29.6% of improvement respect to the planar case. This shows that the filled nanocrosses can produce the main enhancement by themselves, and that a larger density of the pattern produces an additional coupling effect increasing the improvement in a wide S range.

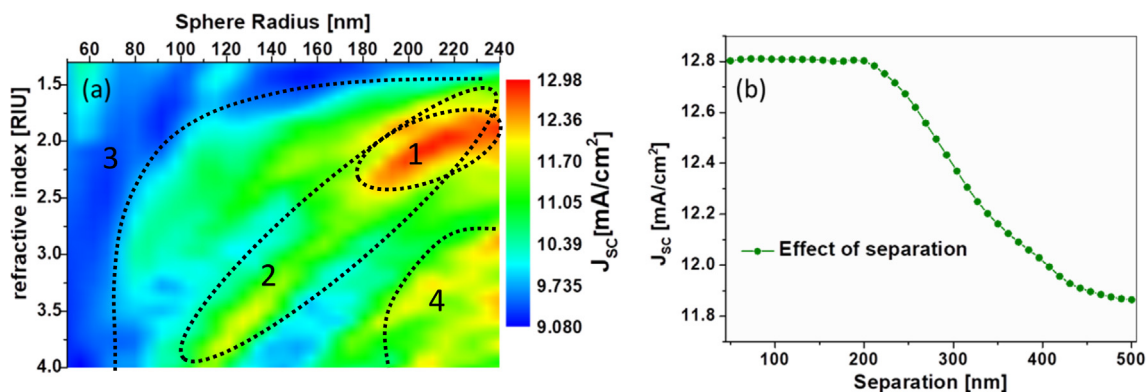Up to now, we have shown that both S and R can have wide

Fig. 2. (a) Sweep in the radius of the nanosphere and refractive index parameters: colors correspond to the generated photocurrent. Separation between crosses is set at $S = 100$ nm. (b) Plot of J_{SC} for the optimized case in (a) respect to the separation between crosses.
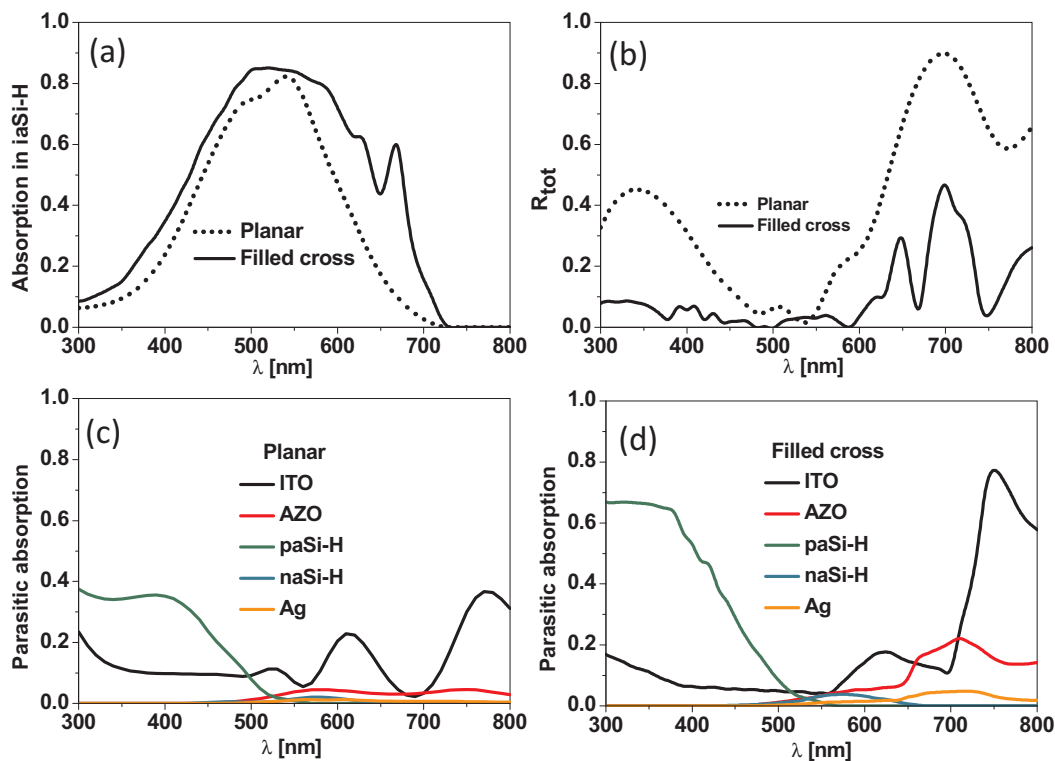
Fig. 3. Analysis of the optimized structure performance: (a) absorption in the active layer and (b) total reflectance; parasitic absorptions in the different layers for the planar (c) and nanostructured (d) cases.

tolerances in fabrication and despite it we can get a much better result than the planar one. Following, we explore the main effects of the proposed metasurface to produce this enhancement.

Fig. 3 provides a closer look to the reason of the enhancement produced by our proposed nanostructure. As Fig. 3a reveals, the proposed nanostructure provides an enhancement of the absorption in the i-aSi:H layer in the whole spectrum respect to the planar case, being the most relevant improvement in the device. This absorption increase is more remarkable at long wavelengths. In this sense, the average absorption in the 300–540 nm interval changes from a 39.8% in the planar case to 49.2% in the proposed one; while the increase in the 540–800 nm goes from a 34.3% to a 55.2%, with a maximum increase at 670 nm. A percent increase of 37.3% in absorption has been reached for the whole 300–800 nm range, which implies the 40% J_{SC} enhancement. The difference between these two values comes from the wavelength dependence of solar spectrum (Eq. (2)), in such a way that the incident number of photons is larger in the second considered range (540–800 nm) (Bai et al., 2010). Thus, the more photons absorbed in that range, the more electron-hole pairs produced.

But the absorption enhancement in the active layer is not the only effect that the proposed metasurface produces in the device performance. Fig. 3b shows the total spectral reflectance for both the planar case and the proposed metasurface in the 300 nm to 800 nm range. As it can be seen, this latter structure provides a decrease in the reflectance for the whole range, with the exception of 540 nm. The reduction of the reflection losses is remarkably higher for the wavelengths above this one. At 700 nm, as the most relevant case, the planar device has a 90% of reflection and the nanocross-nanosphere combination reduces it to a 30%. The improvement of the device performance and its spectral shape is directly related to the light management effects produced by the structure. As we will show, these effects lead the light through it towards the active layer.

Fig. 3c and 3d show the parasitic absorption in the rest of the layers to allow a comparison between the planar and the nanostructured cases, respectively. As stated in the introduction, an absorption in the

auxiliary layers could be advantageous for the performance of the cell, as it could increase the internal temperature, providing a solution for the light induced effects that jeopardize the performance of this kind of cells. Interestingly, comparing the planar and nanostructured cases we can see an increase in the absorption in every layer. Remarkably, the cross pattern in the ITO produces a high increase in the absorption of this layer at the 700–800 nm interval, and a slight decrease in the 600–700 nm interval. The increase is a significant jump, from a 38% to a 77% at their maximum values. The case of AZO is proportionally even more relevant, rising from a 5% to a 20% between the planar and nanostructured case. Among the rest of the aSi transport layers, we get a remarkable increase in the absorption of the p-type one, particularly in the 300–400 nm range, where it jumps from a 35% to a 63%. Finally, Ag back contact, a metal that can provide more heating by absorption due to their inherent properties, gets also an increase in its absorption in the 700 nm region, where we have found the most relevant increase for the majority of the materials.

It is interesting to compare the information coming from Fig. 3b and 3d. We can deduce that the reflectance of the upper layers predominates in the total reflectance below 540 nm, being the wavelength region where the antireflection effects of the structure dominate. But Fig. 3d shows that the parasitic absorption in the p layer is high, so the possible optical improvement is lost. Nevertheless, the absorption in the non-active layers produces an increment in energy dissipation that could induce a self-annealing, reducing the Staebler-Wronski effect. On the other hand, reflection from back layers becomes important in the wavelength region over 540 nm, for which our proposed design produces light-trapping effects that improve the optical absorption in every layer of the device. This can be deduced from the increased absorption both in the amorphous silicon layers and in the ITO and AZO, seen in Fig. 3d.

Until now, it can be seen that the metasurface produces a better operation of the aSi:H solar cell, in particular in the wavelength range from 540 to 800 nm. For this reason, we are going to focus on this spectral region to take an even closer look to what is happening inside
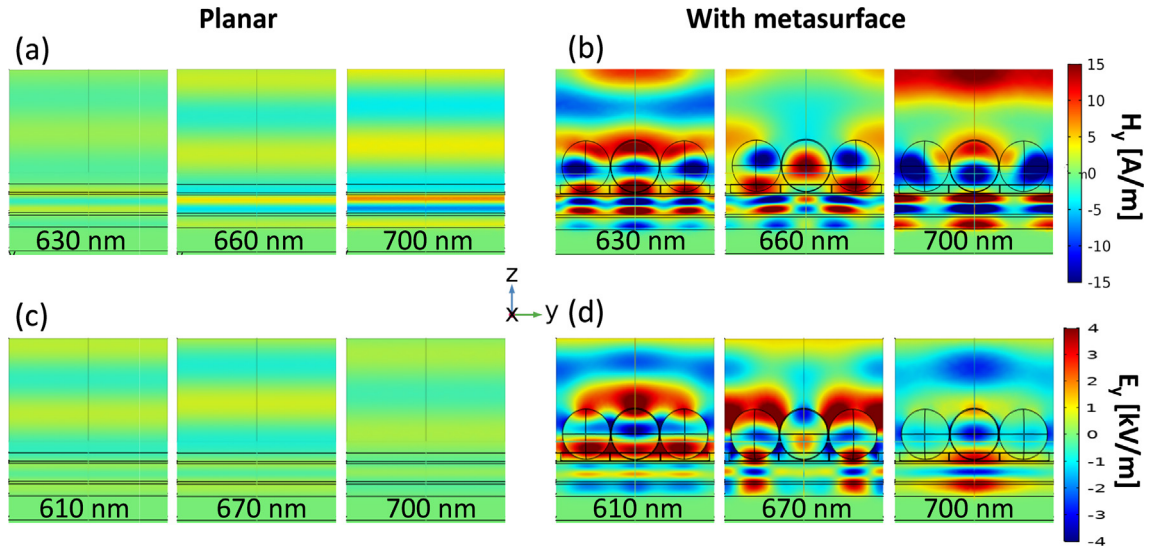
Fig. 4. Top: Spatial distribution of the magnetic field (Hy) considering a TE polarization for a planar (a) and metasurface based (b) solar cell. Same scale. **Bottom**: Spatial distribution of the electric field (Ey) considering a TM polarization for a planar (c) and metasurface based (d) solar cell. Same scale. Wavelengths of larger enhancements in absorption have been selected.

the device. Fig. 4a and 4b show the spatial distribution of the magnetic field (TE polarization) at different layers of both the planar and the proposed solar cell, respectively. Fig. 4c and 4d show the spatial distribution of the electric field (TM polarization) for the same configurations. Light is incoming from above along the z axis in the negative direction in all the cases. For the remaining field distributions, we assume that the symmetry of the system produces similar results. It can be clearly seen in Fig. 4 that for certain wavelengths, those where we found an enhancement in the active layer absorption in Fig. 3, confinement and guiding effects arise in the nanostructured case. This enhances light intensity in the active layer. The field inside the spheres reveals a resonance that is clearly dependent on the wavelength (see Supplementary information). Moreover, the spheres distribution leads the light to focus on the lower layers, mainly in the active one, which must be the origin of the enhancement in their absorption. Here, there are scattering effects due to the spheres shape and size, the refractive index contrast between their dielectric material and the lower layers ones (Algorri et al., 2017; García-Cámara et al., 2013), and their ensemble, effects that have been optimized by the search shown in Fig. 2. Moreover, the use of the dielectric spheres instead of metal ones ensures that there are no further absorption effects that could reduce the light guiding towards the active layer.

At this point, we want to guess an explanation about what part of the produced effects are due to the cross-pattern of ITO and what are due to have filled the crosses with the nanospheres. In an attempt to solve this question, we present in Fig. 5 the photogenerated short-circuit current density in the active layer, J_{SC}, for different cases. We have used a point into the region 1 of the Fig. 2, providing a particle size and refractive index that produces an optimized J_{SC} value. Regarding Fig. 5a, we plot the J_{SC} as a function of the active layer thickness for the planar case, the case in which the cross pattern in the ITO is empty, and the case where the crosses are filled with the ZnO nanospheres. The active layer thickness changes from 50 to 400 nm. This interval is the recommended one to have a good performance, as it was stated in the Introduction section. Indeed, we can see how the trend of the plot is to get a stable value when increasing the thickness. The cross pattern improves the current by itself in a quantity of 1 mA/cm² on average for the whole active layer thickness range. This demonstrates that the patterning of the ITO not only does not reduce but also increases the photogenerated J_{SC}. We can assume also that the carriers extraction will not be affected by it. This can be supported by other results in the literature, where ITO has been patterned and the tradeoff between its

resistance and carrier extraction is maintained. Nanohelix 3D patterns improving a 10% the J_{SC} (Kwon et al., 2014), or lithographically-fabricated cross-micropattern in photodetectors and solar cells (Jeong et al., 2011; Deinega et al., 2013; Sakamoto et al., 2018), are some examples of good results achieved by only nanopatterning ITO.

When filling the crosses with the nanospheres we obtain a remarkable increase in the J_{SC} at the whole range, between 3 and 4 mA/cm² larger than the planar case. This is equivalent to the 40% enhancement that we stated above. Two effects can be deduced from it: first, we can set a certain thickness for the active layer (see vertical black dashed line at Fig. 5a), and obtain a clear enhancement in the generated photocurrent by using the proposed metasurface; second, with this metasurface we can achieve the same J_{SC} value of a planar configuration, but with a much smaller thickness of the active layer (see horizontal dashed line at Fig. 5a). This is a collateral effect that is advantageous in several ways:

- we get a thinner film solar cell,
- we reduce the needed material for the active layer,
- we ensure that the extraction of charges is enhanced, as being the active layer thinner, it could be shorter than the diffusion length of the photogenerated carriers,
- we reduce all the disturbing effects produced by a thicker active layer, as they were shown in the Introduction section.

On the other hand, we have shown in Fig. 5b that our case is not dependent on the solar incidence. As it was also predicted by the discussion of the Introduction, a cross pattern is able to reduce the effects that could arise by the polarization of incoming light. In our case, the simulations for incoming light with TM in orthogonal directions produce the same results. This is the reason of the Fig. 5b trend, where the patterned structures do not affect the angular dependence more than what the planar case does. As it can be seen, the cross-nanostructure filled with spheres maintains the angular dependence of the J_{SC} up to a 60° angle of incoming light. Even more, we can see that it is even better than the planar and cross-pattern ITO cases, as they two begin decreasing at an incident angle of 50°. In this graph we have used an active layer thickness of 150 nm.

4. Conclusions

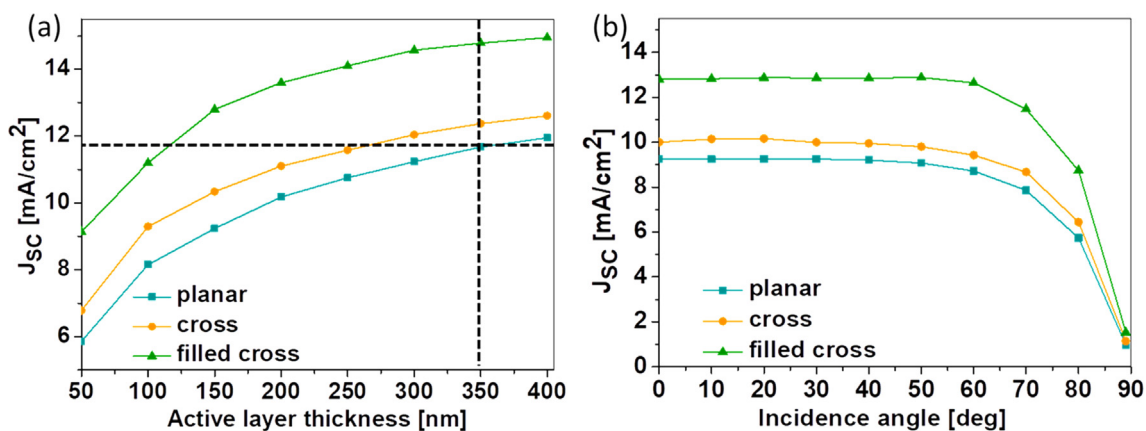This work shows a novel nanostructured solar cell based on aSi:H,

Fig. 5. Photogenerated current for the three cases: planar, ITO cross-patterned and our proposed nanostructure. a: respect to the active layer thickness. b: respect to the incidence angle of light, considering a 150 nm active layer thickness.

where a cross pattern in the upper ITO contact and its filling with dielectric nanospheres produces a remarkable enhancement up to a 40% in the photogenerated short-circuit current density. The effects produced by the nanopattern of crosses and, mainly, the nanospheres location generates a remarkable increase of the light absorption in the active layer and the reduction of the reflection losses of the device. In particular, the nanoparticles produce guiding effects in the incoming light, which focuses on the active layer. The close distance between the spheres and the active layer is crucial to have these effects reinforced.

We have swept different geometrical conditions and materials for the sphere to get a reasonable set of parameters providing an optimum performance. This study has revealed that it is the combination of the cross-shaped pattern and the nanospheres what produces joint diffraction and resonant effects to get that optimum performance. In this sense, small spheres do not produce resonant effects in the wavelengths of interest, while larger spheres combine their resonant effect with the diffraction one due to the nanocross pattern. The pattern itself is producing a reinforcement, as when the crosses move away from each other, the enhancement decays.

The obtained geometrical values and materials are feasible to be manufactured by research groups with nanostructured solar cell fabrication facilities. Indeed, we have a cross pattern in the order of microns, and nanospheres with a 210 nm radius, which are quite practicable to obtain. The selection of ZnO material for the spheres allows the reinforcement of the effects due to its dielectric nature, as well as the refractive index contrast achieved between it and the ones of the layers below.

Using such structure has allowed several effects that are advantageous both for fabrication and for the performance. Among them, the reduction of the thickness of the active layer to get the same photogenerated short-circuit current density than a certain planar case. This particularly produces by itself an enhancement in the charge extraction, due to the increase in the ratio between the diffusion length of the carriers and the length of their path to be extracted from the active layer. Moreover, the reduction of the thickness ensures the reduction of some harmful effects that can be found in the aSi:H literature. Those effects can be removed also with the help of the increase in the absorption at the auxiliary layers, which could increase also the temperature inside the cell and get a long-term annealing to reduce defects.

Declaration of Competing Interest

The authors declare that they have no known competing financial interests or personal relationships that could have appeared to influence the work reported in this paper.

Appendix A. Supplementary material

Supplementary data to this article can be found online at https://doi.org/10.1016/j.solener.2020.03.075.

References:

Agarwal, H., Kumar, S.V., Rajeshkumar, S., 2017. A review on green synthesis of zinc oxide nanoparticles – An eco-friendly approach. Resour-Eff Technol. 3 (4), 406–413.

Agarwal, S.C., Omar, S., 2018. Forty years of the Staebler-Wronski effect. Philos. Mag. 98 (27), 2512–2528.

Amalatas, A.P., Alkaisi, M.M., 2019. Nanostructures for light trapping in thin film solar cells. Micromachines-Basel. 10 (9), 619.

Algorri, J.F., García-Cámara, B., Cuadrado, A., Sánchez-Pena, J.M., Vergaz, R., 2017. Selective dielectric metasurfaces based on directional conditions of silicon nanopillars. Nanomater.-Basel 7 (7), 177.

Algorri, J.F., Zografopoulos, D.C., Ferraro, A., García-Cámara, B., Vergaz, R., Beccherelli, R., Sánchez-Pena, J.M., 2019. Anapole modes in hollow nanocuboid dielectric metasurfaces for refractometric sensing. Nanomater.-Basel 9 (1), 30.

Atwater, H.A., Polman, A., 2010. Plasmonics for improved photovoltaic devices. Nat. Mater. 9 (3), 205–213.

Bai, W., Gan, Q., Song, G., Chen, L., Kafafi, Z., Bartoli, F., 2010. Broadband short-range surface plasmon structures for absorption enhancement in organic photovoltaics. Opt. Express 18 (S4), A620–A630.

Barreda, A.J., Gutiérrez, Y., Alcaraz de la Osa, R., Moreno, F., González, F., 2019a. Optimizing shape characteristics of high refractive index particles to improve scattering. J. Quant. Spectrosc. Radiat. Transfer. 236 106573.

Barreda, A.J., Saiz, J.M., González, F., Moreno, F., Albella, P., 2019b. Recent advances in high refractive index dielectric nanoantennas: Basics and applications. AIP Adv. 9 040701.

Bodurov, I., Vlaeva, I., Viraneva, A., Yovcheva, T., Sainov, S., 2016. Modified design of a laser refractometer. Nanosci. Nanotechnol. 16, 31–33.

Boroumand, J., Das, S., Vázquez-Guardado, A., Franklin, D., Chanda, D., 2016. Unified electromagnetic-electronic design of light trapping silicon solar cells. Sci. Rep. 6, 31013.

Brongersma, M.L., Cui, Y., Fan, S., 2014. Light management for photovoltaics using high-index nanostructures. Nat. Mater. 13, 451–460.

Cao, J., Yang, G., Gu, Y., Fang, X., Lu, N., Hua, B., Yan, X., 2019. Perfect light absorption of monolayer MoS$_2$ with cross-shaped groove air resonator. Mater. Res. Express. 6 015050.

Deinega, A., Eyderman, S., John, S., 2013. Coupled optical and electrical modeling of solar cell based on conical pore silicon photonic crystals. J. Appl. Phys. 113 224501.

Dhouib, A., Filali, S., 1990. Operating temperatures of photovoltaic panels. In: Sayigh, A.A.M. (Ed.), Energy and the Environment, Into the 1990s. Pergamon, UK, pp. 494–498.

Elshorbagy, M.H., García-Cámara, B., López-Fraguas, E., Vergaz, R., 2019. Efficient light

management in a monolithic tandem perovskite/silicon solar cell by using a hybrid metasurface. Nanomaterials-Basel. 9 (5), 791.

Enrichi, F., Quandt, A., Righini, G.C., 2018. Plasmonic enhanced solar cells: summary of possible strategies and recent results. Renew. Sust. Energ. Rev. 82, 2433–2439.

Fujikake, S., Ota, H., Ohsawa, M., Hama, T., Ichikawa, Y., Sakai, H., 1994. Light-induced recovery of a-Si solar cells. Sol. Energy Mater. Sol. Cells. 34, 449–454.

García-Cámara, B., Gómez-Medina, R., Sáenz, J.J., Sepúlveda, B., 2013. Sensing with magnetic dipolar resonances in semiconductor nanospheres. Opt. Express. 21 (20), 23007–23020.

Grandidier, J., Callahan, D.M., Munday, J.N., Atwater, H.A., 2012. Gallium arsenide solar cell absorption enhancement using whispering gallery modes of dielectric nanospheres. IEEE J. Photovolt. 2 (2), 123–128.

Ha, K., Jang, E., Jang, S., Lee, J.K., Jang, M.S., Choi, H., Cho, J.S., Choi, M., 2016. A light-trapping strategy for nanocrystalline silicon thin-film solar cells using three-dimensionally assembled nanoparticle structures. Nanotechnology 27 055403.

Jang, S., Yoon, J., Ha, K., Kim, M., Kim, D.H., Kim, S.M., Kang, S.M., Jung, H.S., Choi, M., 2016. Facile fabrication of three-dimensional TiO_2 structures for highly efficient perovskite solar cells. Nano Energy 22, 499–506.

Jeong, H., Kim, K.S., Kim, Y.H., Jeong, H., Song, H., Lee, K.H., Jeong, M.S., Wang, D., Jung, G.Y., 2011. A crossbar-type high sensitivity ultraviolet photodetector array based on a one hole–one nanorod configuration via nanoimprint lithography. Nanotechnology 22 275310.

Khan, A.D., Rehman, Q., Khan, A.D., Subhan, F.E., Noman, M., Ahmed, S., Khan, A.H., 2019. Broadband solar energy absorption in plasmonic thin-film amorphous silicon solar cell. Coatings 9, 638.

Khoshdel, V., Joodaki, M., Shokooh-Saremi, M., 2019. UV and IR cut-off filters based on plasmonic crossed-shaped nano-antennas for solar cell applications. Opt. Commun. 433, 275–282.

Könenkamp, R., Muramatsu, S., Itoh, H., Matsubara, S., Shimada, T., 1990. Mobility-lifetime product in hydrogenated amorphous silicon. Jpn. J. Appl. Phys. 29, L2155–L2158.

Kwon, H., Ham, J., Kim, D.Y., Oh, S.J., Lee, S., Oh, S.H., Schubert, E.F., Lim, K.G., Lee, T.W., Kim, S., Lee, J.L., Kim, J.K., 2014. Three-dimensional nanostructured indium-tin-oxide electrodes for enhanced performance of bulk heterojunction organic solar cells. Adv. Energy Mater. 4 (7), 1301566.

Lee, S.H., Ha, N.Y., 2011. Nanostructured indium-tin-oxide films fabricated by all-solution processing for functional transparent electrodes. Opt. Express. 19 (22), 21803–21808.

Li, R., Li, B.Q., Wang, W., 2019. Forward scattering nanoparticles-based nanostructure for light trapping over solar spectrum. AIP Adv. 9 085119.

Luo, Q., Deng, X., Zhang, C., Yu, M., Zhou, X., Wang, Z., Chen, X., Huang, S., 2018. Enhancing photovoltaic performance of perovskite solar cells with silica nanosphere antireflection coatings. Sol. Energy 169, 128–135.

Morawiec, S., Mendes, M.J., Priolo, F., Crupi, I., 2019. Plasmonic nanostructures for light trapping in thin-film solar cells. Mat. Sci. Semicon. Proc. 92, 10–18.

NREL: National Renewable Energy Laboratory. MS Excel™ spreadsheet file. Available online: https://rredc.nrel.gov/solar/spectra/am1.5 (accessed on July 20th, 2019).

Pola, I., Chianese, D., Fanni, L., Rudel, R., 2008. Analysis of annealing and degradation effects on a-Si modules. In: Proc. 23rd European Photovoltaic Solar Energy Conference and Exhibition, Valencia, Spain, pp. 2301–2304.

Sakamoto, K., Kuwae, H., Kobayashi, N., Nobori, A., Shoji, S., Mizuno, J., 2018. Highly flexible transparent electrodes based on mesh-patterned rigid indium tin oxide. Sci. Rep. 8, 2825.

Shiri, A., Villinger, M.L., Shabahang, S., Jahromi, A.K., Villinger, C.H., Abouraddy, A.F., 2019. Broadband omni-resonance doubles the near-infrared quantum-efficiency of a thin film solar cell, in frontiers in optics + laser science APS/DLS, OSA Technical Digest (Optical Society of America, 2019), paper JW4A.83.

Spinelli, P., Verschuuren, M.A., Polman, A., 2012. Broadband omnidirectional antireflection coating based on subwavelength surface Mie resonators. Nat. Commun. 3, 692.

Staebler, D.L., Wronski, C.R., 1977. Reversible conductivity changes in discharge-produced amorphous Si. Appl. Phys. Lett. 31, 292–294.

Son, J.G., Bae, W.K., Kang, H., Nealey, P.F., Char, K., 2009. Placement control of nanomaterial arrays on the surface-reconstructed block copolymer thin films. ACS Nano 3 (12), 3927–3934.

Terekhov, P.D., Babicheva, V.E., Baryshnikova, K.V., Shalin, A.S., Karabchevsky, A., Evlyukhin, A.B., 2019. Multipole analysis of dielectric metasurfaces composed of nonspherical nanoparticles and lattice invisibility effect. Phys. Rev. B. 99 045424.

Vashistha, V., Vaidya, G., Hegde, R.S., Serebryannikov, A.E., Bonod, N., Krawczyk, M., 2017. All-dielectric metasurfaces based on cross-shaped resonators for color pixels with extended gamut. ACS Photonics 4, 1076–1082.

Vaskin, A., Kolkowski, R., Koenderink, A.F., Staude, I., 2019. Light-emitting metasurfaces. Nanophotonics-Berlin 8 (7), 1151–1198.

Vismara, R., Odebo Länk, N., Verre, R., Käll, M., Isabella, O., Zeman, M., 2019. Solar harvesting based on perfect absorbing all-dielectric nanoresonators on a mirror. Opt. Express 27 (16), A967–A980.

Vora, A., Gwamuri, J., Pearce, J.M., Bergstrom, P.L., Güney, D.Ö., 2014. Multi-resonant silver nano-disk patterned thin film hydrogenated amorphous silicon solar cells for Staebler-Wronski effect compensation. J. Appl. Phys. 116 (9) 093103.

Wang, B., Gao, T., Leu, P.W., 2016. Broadband light absorption enhancement in ultrathin film crystalline silicon solar cells with high index of refraction nanosphere arrays. Nano Energy 19, 471–475.

Xia, D., Brueck, S.R.J., 2004. Lithographically directed deposition of silica nanoparticles using spin coating. J. Vac. Sci. Technol. B. 22 (6), 3415–3420.

Zaidi, Z., Siddiqui, S.I., Fatima, B., Chaudhry, S.A., 2019. Synthesis of ZnO nanospheres for water treatment through adsorption and photocatalytic degradation: Modelling and process optimization. Mat. Res. Bull. 120 110584.

Zou, C., Sautter, J., Setzpfandt, F., Staude, I., 2019. Resonant dielectric metasurfaces: active tuning and nonlinear effects. J. Phys. D: Appl. Phys. 52 373002.